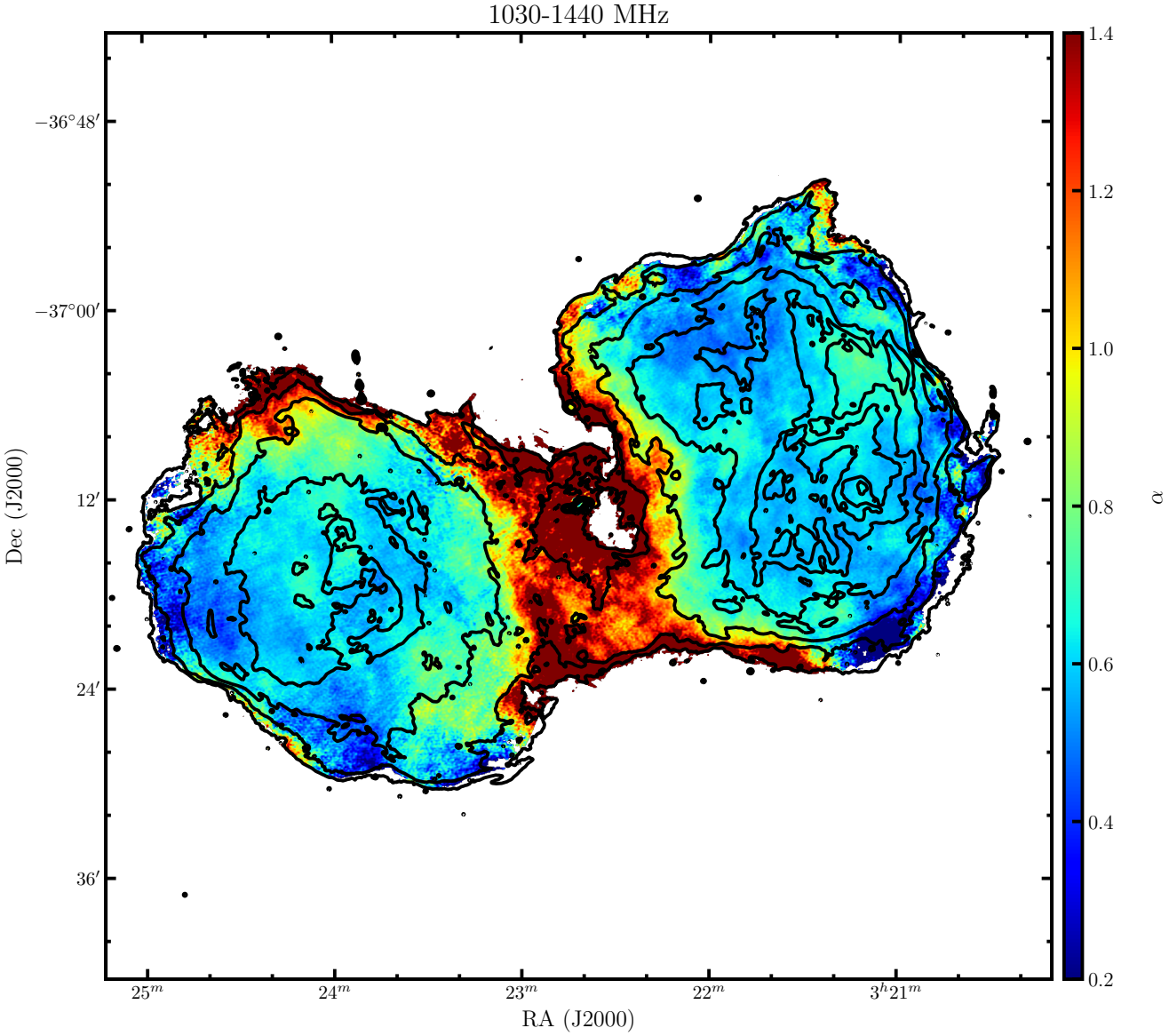

Fig. 9. Spectral index map of the radio emission of Fornax A between 1.03 GHz and 1.44 GHz. The resolution of the map is $10'' \times 10''$. The contour levels show the radio emission at 1.44 GHz. They start at 0.8 mJy beam^{-1}, increasing by a factor of two.

6.1. The lobes

The total intensity map does not show any clear evidence of a hot-spot or a jet expanding through the lobes. In the spectral index map (Fig. 9) we identify three main components with different spectral indexes. The centre of the lobes, which has an overall spectral index of ∼0.7. The "bridge" connecting the lobes and the inner edges of the lobes (i.e. the edges closer to the host galaxy and in the north of the east lobe and south of the west lobe, respectively) have steep spectrum ($\alpha \sim 1.3$) and the outer edges which have flat spectrum ($\alpha \lesssim 0.5$).

The spectral index map between two close frequencies from the same observation can provide a limited view of the spectral shape of the synchrotron emission. The calibration of the observation, radio frequency interference, and the uv-coverage of the observation are all effects that may contribute to slightly change the flux distribution in the images, and therefore may bias the spectral index map. For these reasons we also create spectral index maps between 200 MHz and 1.44 GHz, between 1.03 GHz and 6.3 GHz, and between 200 MHz and 6.30 GHz. For this analysis we convolve all images to the resolution of $3' \times 3'$, which matches the resolution of the MWA and SRT images. We do not consider the *Planck* observations because they resolve the lobes with only two resolving beams at most, and this does not allow us to trace the differences in spectral index within the lobes. The results are shown in Fig. 10. The main spectral features shown in the high-resolution map are also recovered in these maps, namely the steep (∼1) spectral index in the centre and in the bridge, and an overall uniform spectral index in the lobes (∼0.7). Some regions at the edges of the lobes show a flatter spectrum.

The $\mathrm{CI_{OFF}}$ models provide a good description of the injection history of the lobes of Fornax A considered as a whole. Nevertheless, these components are resolved by our observations, and it is possible to trace the differences in radiative age within the lobes. The continuous injection of particles into the lobes can be thought of as the sum of subsequent injections between the time zero and the time t_{CI}, whose individual radiative losses are well described by the JP model (see Sect. 5). Since the $\mathrm{CI_{OFF}}$ model provides a good description of the overall injection history of the

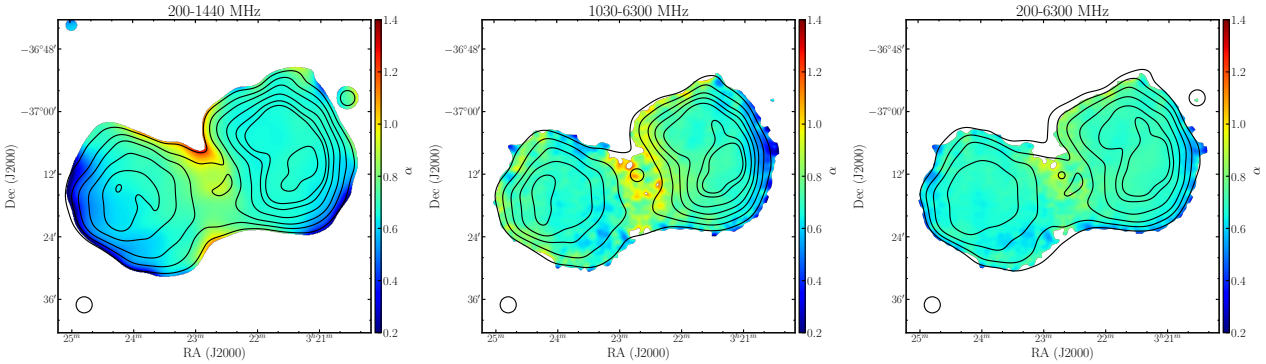

Fig. 10. *Left panel*: spectral index map of Fornax A between 200 MHz and 1.44 GHz (extracted from MWA and MeerKAT observations). The resolution is the same in all images ($3' \times 3'$) and is shown in black in the bottom left corner. The colour scale is the same as in Fig. 9. The contour levels show the radio emission at 1.44 GHz. Contours start at 0.1 mJy beam^{-1}, increasing by a factor of two. *Central panel*: spectral index map between 1.03 GHz and 6.30 GHz (taken from MeerKAT and SRT observations). The colour-scale of the map is the same as in the left panel. The contour levels show the radio emission at 1.03 GHz, starting at 0.2 mJy beam^{-1}, increasing by a factor of two. *Right panel*: spectral index map between 200 MHz and 6.3 GHz (from MWA and SRT observations). The PSF and colour-scale of the map are the same as in the top left panel. The contour levels show the radio emission at 200 MHz, starting at 0.5 mJy beam^{-1}, increasing by a factor of two.

lobes, by tracing the spectral differences through the lobes, we expect to identify some regions where the break-frequency of the best-fit JP model has values close to $\nu_{\rm break,\,high}$ and others where the break-frequency is as low as $\nu_{\rm break}$.

We measure the flux density in different regions of the lobes of Fornax A between 200 MHz and 6.30 GHz on the images convolved at $3' \times 3'$. The regions are of the same size as the point spread function (PSF) and are selected to be located more or less symmetrically in both lobes. We select regions close to the centre ($E_{\rm c}$, $W_{\rm c}$, $W_{\rm c2}$), along the apparent direction of expansion of the radio jets ($E_{\rm j}$, $W_{\rm j}$), at the edges ($E_{\rm h}$, $W_{\rm h}$, $E_{\rm s}$, $W_{\rm s}$, $E_{\rm n}$, $W_{\rm n}$), and one region in the bridge. These regions are shown in the spectral index map of Fig. 11. The panels of this figure show the best-fit JP model to the spectrum of each region. The pattern visible in the 1.03–1.44 GHz spectral-index image (Fig. 9) is visible also now that we model the flux density over a broader band even if at lower angular resolution. The regions with a higher break are in the north and south edge of the west lobe ($W_{\rm n}$ and $W_{\rm s}$) and in the east and south edge of the east lobe (the $E_{\rm h}$ and $E_{\rm s}$), while the centre and the bridge show low breaks. The panels in Fig. 11 confirm that the break-frequency is high throughout the lobes, and that the *Planck* non-detection of the lobes at frequencies $\gtrsim$143 GHz does not bias this result. Nowhere in the lobes can we observe a pure power-law spectrum. This confirms that the lobes of Fornax A are likely not currently active.

The regions with flat spectrum (such as $E_{\rm h}$, $W_{\rm s}$, $W_{\rm n}$, $W_{\rm c2}$) correspond to some of the low-polarisation patches identified by Anderson et al. (2018). In these regions, the associated Faraday depth enhancement may be due to magnetised plasma residing in the lobes, and advected from the host galaxy ISM during their expansion. Regions $E_{\rm h}$ and $W_{\rm n}$ also coincide with a peak in the hard X-ray distribution (see Fig. 1b in Kaneda et al. 1995).

It is possible to generate the break-frequency map of the radio emission of the lobes of Fornax A from the spectral index map. Myers & Spangler (1985) show that from Eqs. (9) and (10) the radio spectral index between two frequencies is a function of the ratio between the frequency where the spectral index is measured and the break frequency. The relation between the two-frequency spectral index and the break frequency diverges for large values of the spectral index or when it is close to zero. For pixels with $\alpha \gtrsim 1.4$ or pixels with $\alpha \lesssim 0.2$ the estimated break frequencies should be considered as lower and upper limits, respectively. The break-frequency map generated following this method is shown in Fig. 12. The outer edges of the lobes have a high break frequency ($\gtrsim$220 ± 140 GHz) while the inner edges and the bridge have the lowest breaks ($\lesssim$50 ± 5 GHz). In the centre of the lobes, overall, the break frequency is ∼130 ± 40 GHz. This value is very close to the $\nu_{\rm break,\,high}$ of the best fit CI$_{\rm OFF}$ model of the total flux density of the lobes.

6.2. The central emission

The left panel of Fig. 13 shows the central region of the spectral index map between 1.03 GHz and 1.44 GHz. Regions with flat spectrum are located close to the kpc-core, while the spectrum steepens moving along the jets. In the right panel, we show the corresponding break-frequency map. The edges of the jets have the lowest break frequency ($\nu_{\rm break} \lesssim 50$ GHz), while the kpc-core has a high break frequency. This is in good agreement with the spectra of the jets and kpc-core (Fig. 8), which suggest that the jets have not been replenished with energetic particles for most of their lifetime.

The indications given by the map of break frequency confirm what was previously observed in the spectral index map between the VLA observations at 4.9 and 14.9 GHz (Ekers et al. 1983; Geldzahler & Fomalont 1984) that attributed the steepening of the spectral index in the jets to their radiative ageing.

7. Discussion

7.1. The formation of the radio lobes

The properties of the flux density spectrum of the lobes of Fornax A are puzzling when compared to their projected size. Typically, lobes extending in the IGM for hundreds of kiloparsecs are either the remnant of an old nuclear activity, and show a steep spectrum with low break frequency, or they are currently being injected with relativistic particles and show a jet or stream of particles connecting the AGN with the lobes. In the previous section, we showed that the most remarkable properties of the lobes of Fornax A are the flat spectral shape and high break frequency ($\gtrsim$20 GHz) of their radio emission, and that the nuclear activity that was replenishing the lobes with high-energy particles was short (∼24 Myr) and had recently stopped (∼12 Myr ago). The main open question therefore pertains to how these large lobes have formed in such a short time.

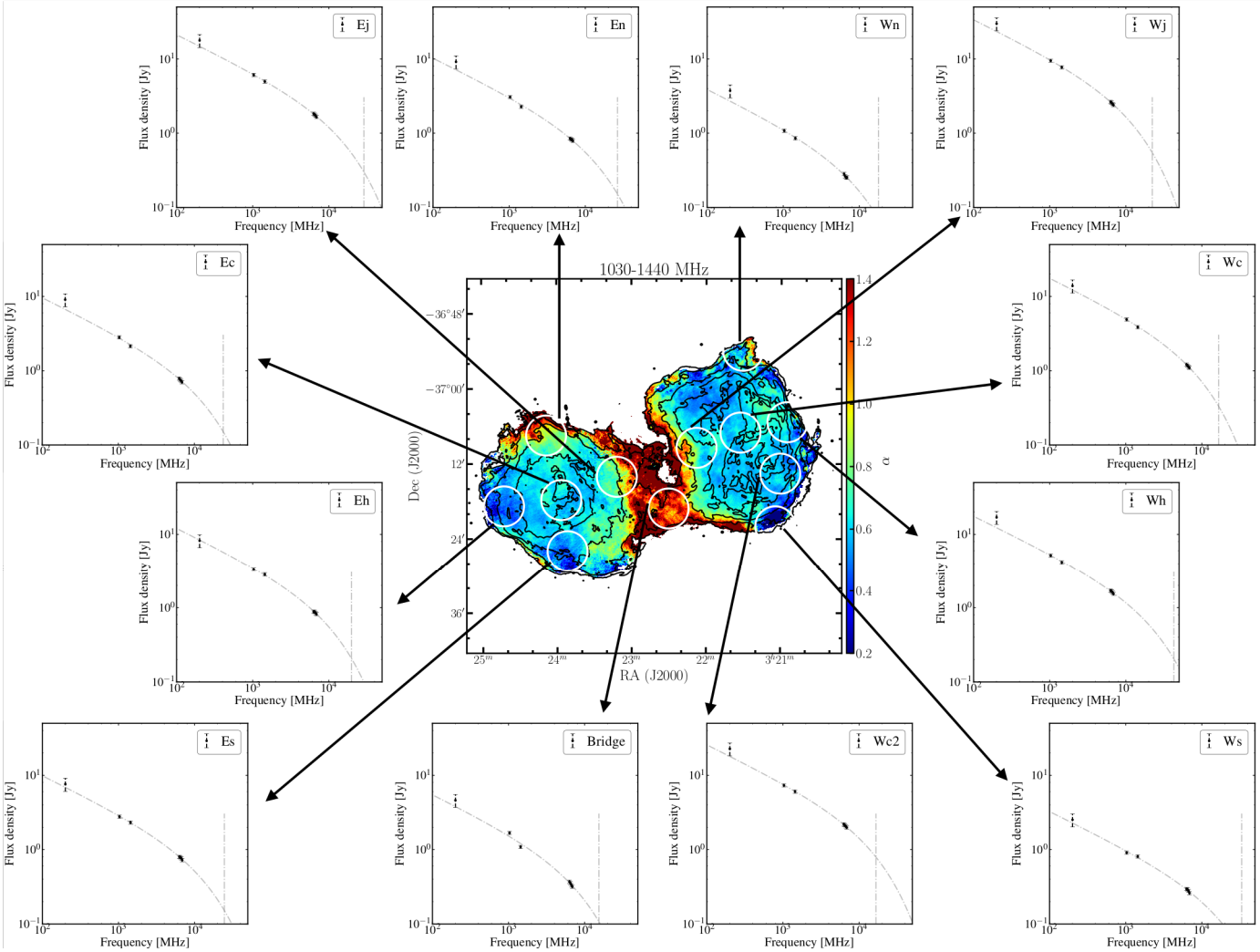

Fig. 11. Spectral index map of the radio emission of Fornax A. The white circles mark the regions where we analyse the spectral differences within the lobes. The panels show the best fit JP model for the spectra of each region (further details are given in Sect. 6). Regions at the edge of the lobes have a higher break frequency than the bridge and the inner regions.

We estimate a dynamical age for the lobes of Fornax A by assuming that their expansion was transonic. If the energy density of the relativistic fluid is comparable to that of the IGM, the lobes may have expanded at the speed of sound:

$$c_{\rm s} = \sqrt{\Gamma_{\rm gas} \frac{k_{\rm BT}}{\mu m_{\rm h}}}, \tag{13}$$

where $\Gamma_{\rm gas} = 5/3$, $\mu = 1$ is the mean molecular weight of the gas, and $k_{\rm B}$ and $m_{\rm h}$ are the Boltzmann's constant and the mass of the hydrogen atom, respectively. Given that the temperature (T) of the IGM surrounding Fornax A ($60 < r < 350$ kpc) is $\sim 2.7\times10^7$ K ($\sim$0.65–0.77 keV, as measured from the X-ray emission of the hot halo of NGC 1316; Isobe et al. 2006; Nagino & Matsushita 2009; Gaspari et al. 2019), the speed of sound is $c_{\rm s} = 529\,{\rm km\,s^{-1}}$. If the lobes expanded through the IGM at this speed, it would have taken $\sim$200 Myr to reach their current size. As shown in Fig. 14, this age is one order of magnitude larger than the radiative age inferred from the break frequency of the spectrum of the lobes ($\sim$24 Myr).

To estimate the error on the dynamical expansion, we assumed that its speed could range between double the speed of sound ($1058\,{\rm km\,s^{-1}}$) and half of it ($\sim 264\,{\rm km\,s^{-1}}$); this corresponds to a change in the temperature of the IGM by a factor of four. The lower limit is close to the buoyancy speed used to estimate the age of the X-ray cavities detected between the lobes and the central emission of Fornax A (Lanz et al. 2010). The upper limit of the dynamical age of the radio lobes is $\sim$400 Myr and the lower limit is $\sim$90 Myr. In order for the dynamical age to be compatible with the radiative age, the temperature of the IGM must be at least one order of magnitude larger ($\sim 10^8$ K), which is not compatible with the X-ray measurements of the IGM of Fornax A. These high temperatures are typical of cluster environments, such as for example Virgo A, where a rapid supersonic dynamical inflation has been observed (M 87; de Gasperin et al. 2012). Conversely, Fornax A is located at the edges of the Fornax cluster, where the IGM is much cooler (Gaspari et al. 2019).

We point out that the radiative age we infer from synchrotron radiation is maximal when the magnetic field is close to the field of equipartition ($B_{\rm eq}/\sqrt{3}$; Murgia et al. 2012). As shown in Fig. 14, the magnetic field in the lobes ($B_{\rm eq} = 2.6 \pm 0.3\,\mu$G; Isobe et al. 2006; Tashiro et al. 2009) is very close to the value for which the radiative age is maximal.

Figure 14 indicates that the radiative age of the lobes of Fornax A and the dynamical age are incompatible. It is possible

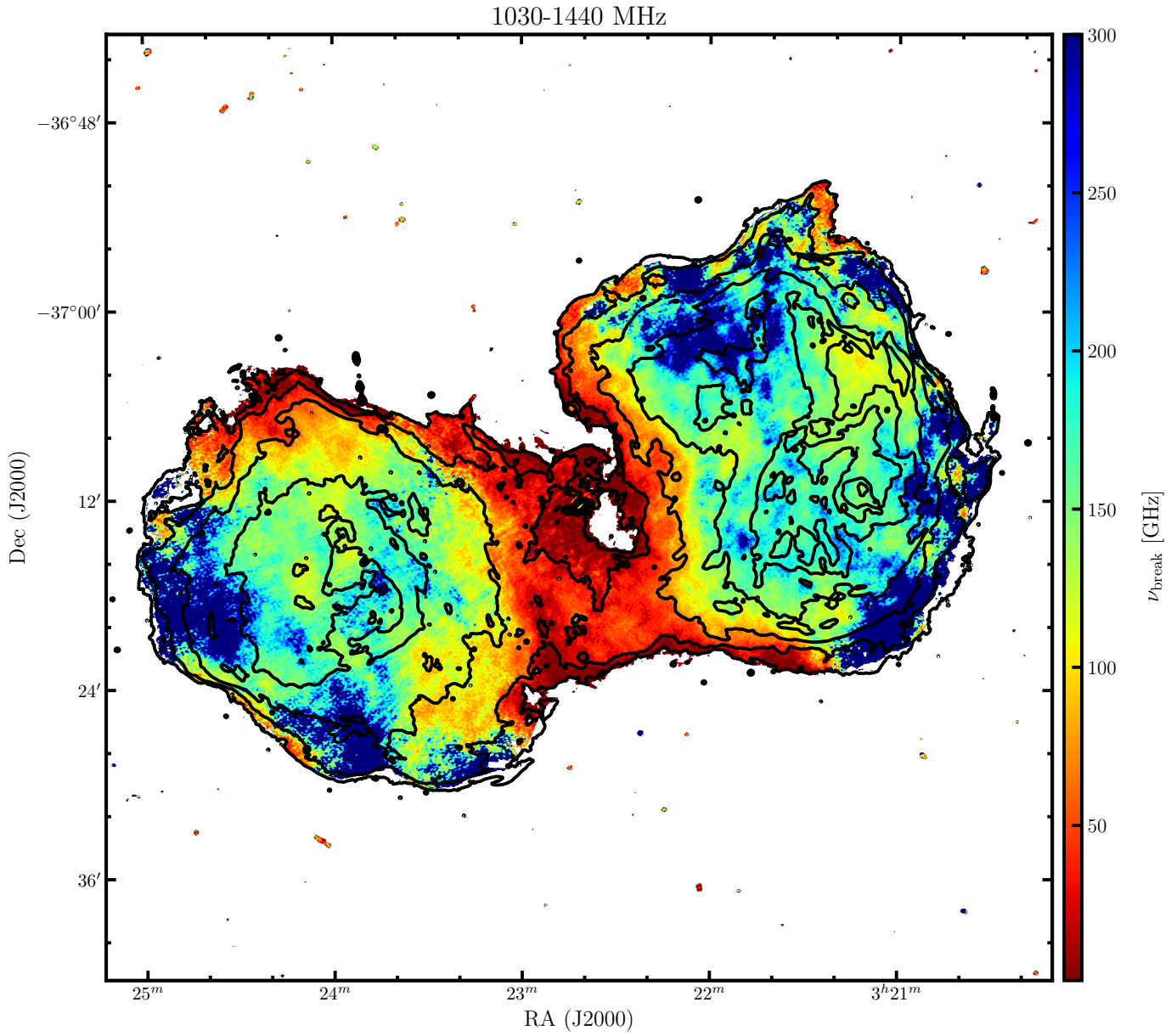

Fig. 12. Break-frequency map inferred from the spectral index map shown in Fig. 9. The PSF of the map is 10″ × 10″. Contour levels show the 1.44 GHz radio emission.

that in a single powerful episode of nuclear activity, supersonic jets carved their way through the IGM and shaped the lobes of Fornax A as we see them now. This phase recently stopped, which would explain the absence of jets and or hot-spots and the spectral shape of the lobes. The main argument disfavouring this solution is the axial ratio of the lobes. This is defined as the length of both lobes divided by the total extent of the source (Leahy & Williams 1984). Typically, in AGNs where the radiative age of the particles of the lobes is similar to their dynamical time of expansion the axial ratio is low (Hardcastle & Worrall 2000; Mullin et al. 2008), while it is close to unity in Fornax A.

Another possibility is that the lobes of Fornax A formed through multiple episodes of activity and that we currently observe the remnant of the last phase, which started approximately 24 Myr ago and was interrupted 12 Myr ago. If the lobes, filled with low-energy particles and under-pressured with respect to the surrounding IGM, were already present because of previous activities, a new nuclear phase may rapidly fill them with new high-energy particles which now dominate the radio emission of the source. This scenario would explain the overall flat radio spectrum of Fornax A and its high break-frequency. Although the low-energy particles, remnants of the previous phases, are dominating the number density of the lobes, they may be negligible in the flux density for two reasons: First, while the source is not active, the particles expand in the IGM losing energy and shifting to lower frequencies. Second, any new injection collects the most energetic particles at the edge of the lobes sweeping away the low-energy ones. This may also explain the double-shell structure of the lobes of Fornax A. The high-energy particles collect at the outer edge of the lobes (which shows flat spectrum), while the less energetic (and older) particles are swept away in a back-flow. This is formed by the inner edges of the lobes and the bridge, which both show a steep spectrum (see Fig. 9). Two separate AGN outbursts have also been proposed by Lanz et al. (2010) to explain the location of the X-ray

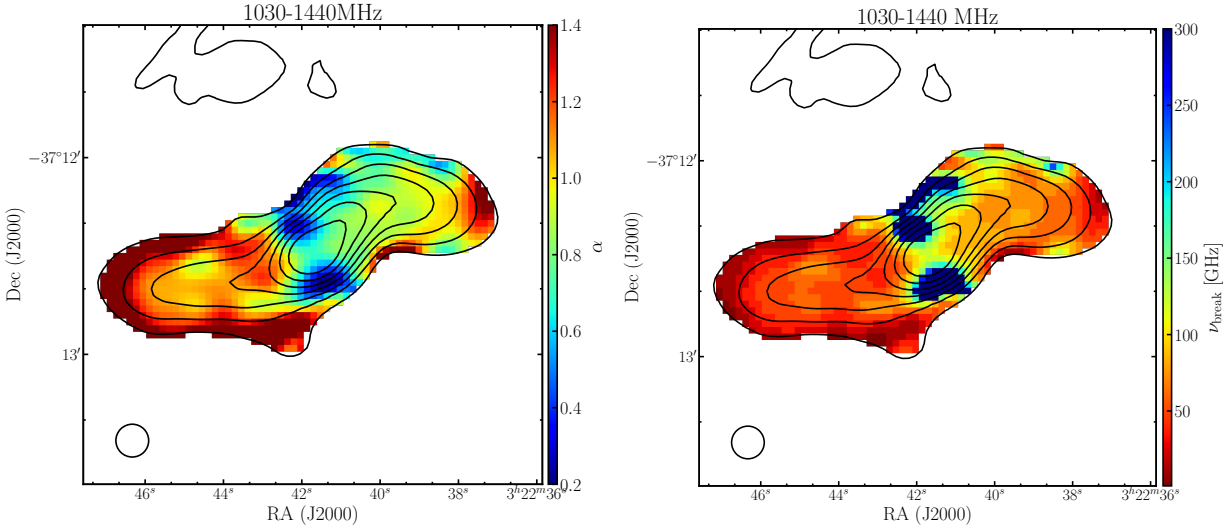

Fig. 13. *Left panel*: spectral index map between 1.03 and 1.44 GHz of the central emission of Fornax A. The resolution ($10'' \times 10''$) is shown in the bottom left corner. The black contours show the 1.03 GHz flux density, starting at 0.6 mJy beam^{-1} and increasing by a factor of two. *Right panel*: break-frequency map of the central emission of Fornax A. The PSF of the map ($10'' \times 10''$) is shown in the bottom left corner. Contour levels are the same as in the left panel.

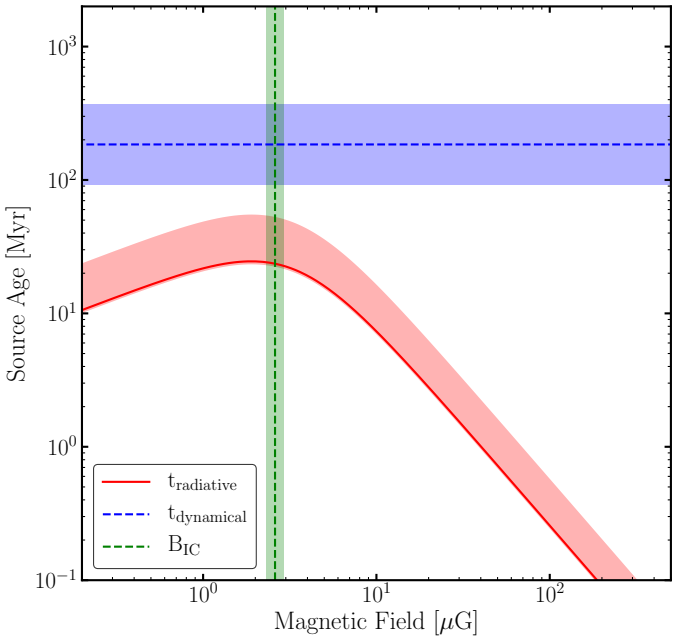

Fig. 14. Comparison of radiative and dynamical age of Fornax A as a function of the magnetic field. The radiative age (red shaded region) is derived from the spectral break measured in the two lobes. The dynamical age is shown in blue. The green region shows the magnetic field measured in the lobes from X-ray inverse Compton emission ($B_{IC} \sim 2.6 \pm 0.3\,\mu$G).

cavities relative to the radio lobes of Fornax A. The formation process of the lobes of Fornax A may have been similar to that of Hercules A. This galaxy shows no clear indication of hot-spots in the lobes, and their double-shell lobe structure has been interpreted as a new activity replenishing high-energy particles in the cocoon, remnant of the previous activity (Gizani & Leahy 2003).

Different episodes of activity would also explain why it is difficult to classify Fornax A as a FRI or a FR II galaxy (Fanaroff & Riley 1974). Its low R parameter ($R = S_{\rm kpc-core}/(S_{\rm tot} - S_{\rm kpc-core}) = 4 \times 10^{-4}$), the non-beamed jets, and a lack of hot-spots in the lobes would classify Fornax A as a FRI source (Morganti et al. 1993). However, the [O III] luminosity is too low for FRI sources (7.96×10^{-15} erg s^{-1} cm^{-2}; Tadhunter et al. 1993) and most of the flux is included in the extended lobes, as is common in FRII galaxies. Likely, the first phase of activity that formed the lobes was much more powerful than the activity of the central emission. Another explanation of the difficulty in classifying Fornax A as an FRI/FRII galaxy may be that, because of the peculiar motions of the host galaxy and of the lobes in the ISM, the galaxy moved away from where it was inflating the lobes (Ekers et al. 1983). If at the time of the last inflation the galaxy was located where the bridge is, then the flatter-spectrum regions at the edges of the lobes could be the remnants of the hotspots of a past FRII activity. Nevertheless, the relative velocity between the galaxy and the lobes would be very high (~2450 km s^{-1}), because the last inflation stopped 12 Myr ago and during this time the galaxy should have moved approximately 30 kpc.

Emission from proton–proton (p–p) collisions of cosmic rays with the thermal plasma within the filaments of the lobes of Fornax A, along with inverse Compton scattering, has been invoked to explain the properties of the radio, X-ray, and γ-ray emission of Fornax A (Seta et al. 2013; McKinley et al. 2015; Ackermann et al. 2016). In the radio band, emission arising from hadronic collisions should result in a single power law spectrum at radio frequencies (see Eq. (9) in Dolag & Enßlin 2000). In Fornax A, the radio lobes show a clear curvature in the total spectrum (Figs. 7 and 15), as well as in most regions within the lobes (at the resolution of 3′, see Sect. 6.1 and Fig. 11). A single power law does not accurately describe the spectral shape of the lobes of Fornax A, which suggests that hadronic collisions are not the dominant process characterising their radio emission. The only exception may be region W_s (see Fig. 11) which shows the highest break frequency and the flattest spectrum of the west lobe. Interestingly, this region coincides with the peak of the γ-ray emission (Ackermann et al. 2016). There, it is possible that interactions between the relativistic plasma and high-energy particles of the IGM are occurring, as suggested by McKinley et al. (2015).

7.2. The flickering activity of Fornax A

In Sect. 5, we studied the radio spectrum of the lobes, and central emission of Fornax A. We measured the injection index and break-frequency from which we estimated the total radiative age of the lobes and central jets and examined whether these components are still being injected with relativistic particles. Given our results, we are now in a position to provide a timescale for the nuclear activity of Fornax A.

In Fig. 15, we show the flux density distribution of the east and west lobes and of the kpc-core and jets. The dashed lines show the best-fit model to the spectra. For the jets and lobes the best-fit model is the $\mathrm{CI_{OFF}}$ model, with similar injection index ($\alpha_{\rm inj} \sim 0.6$), while the kpc-core is best described by the CI model. From the spectral modelling, we derive a total radiative age for the lobes of ∼24 Myr, showing that they have not been injected with relativistic particles for the last 12 Myr. The jets show a total radiative age of ∼3 Myr and have been off for most of their lifetime ($t_{\rm OFF}/t_{\rm s} = 0.89$). These radiative ages seem to indicate that the AGN turned on again for a very short phase ($\lesssim$1 Myr), when the lobes had been off for already ∼9 Myr. The spectral index and break frequency maps (Fig. 13) confirm that the radiative age of the jets increases radially, with the younger regions closer to the kpc-core, and suggest that the nuclear activity that generated the jets was a short, low-power episode where the plasma ejected by the AGN remained confined in the centre of the galaxy ($r \lesssim 6$ kpc). Given the short timescales of the different nuclear activities, Fornax A is likely to be flickering rapidly between an active phase and a non-active one.

Another argument in favour of the multiple nuclear activities of Fornax A is given by the location of the jets and lobes in the jet-core luminosity function of radio AGNs (Parma et al. 1987). The ratio between the jet power and kpc-core power fits nicely in the jet-core luminosity function for objects of this radio power. The ratio between the total radio power ($\sim 2.0 \times 10^{25}$ W Hz^{-1}, dominated by the emission of the lobes) and the jet radio power is low for a source of this luminosity, and this would make Fornax A an outlier in the jet radio luminosity function.

Currently, the central nucleus may be in a new active phase, as suggested by the flat spectral shape of the kpc-core, compatible with the CI model (Fig. 8). In the centre of Fornax A, Parkes-Tidbinibilla interferometric (PTI) observations (Jones et al. 1994; Slee et al. 1994) did not detect any emission at 2.2 and 8.4 GHz over scales of 90 and 27 mas (∼10 pc and 3 pc, respectively) down to 1σ-noise levels of 3 and 6 mJy, respectively. This corresponds to a brightness temperature of $\sim 10^5$ K suggesting that at the time of the observations the radio emission of the core of Fornax A was very weak ($\lesssim 2.0 \times 10^{20}$ W Hz^{-1}). It is possible that the core of Fornax A is variable over short timescales, and new sub-arcsecond resolution observations may provide further insight into its activity.

The radio emission of Fornax A allows us to distinguish three phases of nuclear activity, the one that last injected the lobes, the one that formed the jets, and that of the kpc-core. In the previous section, we suggested that a possible explanation for the axial-symmetry of the lobes and their flat spectral index and high break frequency could be that we are currently observing only the last episode of injection, but that multiple episodes of activity may have occurred in the past. This further corroborates the interpretation that the nuclear activity of Fornax A is flickering. The recurrent activity of Fornax A may fit well in the theoretical scenario of AGN evolution whereby the central engine is active for short periods of time (10^{4-5} years), and that these phases recursively occur over the total lifetime of the AGN (10^8 years; e.g. Schawinski et al. 2015; King & Nixon 2015; Morganti 2017).

The environment in which Fornax A is embedded likely plays a crucial role in regulating its flickering nuclear activity. NGC 1316 is a merger remnant and the most massive early-type galaxy of a group falling into a cluster. The same MeerKAT observation used in this paper was analysed for spectral lines by Serra et al. (2019), leading to the conclusion that the merger occurred between a dominant, gas-poor lenticular and an approximately ten times smaller Milky Way-like galaxy. The cold ISM of this smaller progenitor was partly expelled out to a large radius along tidal tails ($M_{\rm H\,I} \sim 7 \times 10^8\,M_\odot$) and partly flowed towards the centre ($M_{\rm H\,I} \sim 4 \times 10\,M_\odot$). There, it is now mostly found in molecular form ($6 \times 10^8\,M_\odot$ Horellou et al. 2001; Morokuma-Matsui et al. 2019), and has triggered a burst of star formation (Kuntschner 2000; Silva et al. 2008) at about the same time as the formation of the globular clusters (1–3 Gyr ago; Goudfrooij et al. 2001; Sesto et al. 2016, 2018). This merger may have triggered first the AGN for the first time, but is not responsible for the most recent (∼24 Myr) episode of injection of the lobes that we observe now.

After the major merger, NGC 1316 went through several accretion events and minor mergers of smaller companions (Iodice et al. 2017), for which, at this stage, we do not know the typical gas content. These numerous interactions may have regulated the switching on and off of the multiple episodes of activity that formed the lobes as we see them now. Merger and interaction events are often invoked to explain the triggering of powerful AGNs (e.g. Heckman et al. 1986; Hopkins et al. 2005; Ramos Almeida et al. 2012; Sabater et al. 2013). Chaotic accretion of cold clouds is also an efficient mechanism to trigger and regulate the recurrent activity of AGNs (e.g. Gaspari et al. 2013; King & Nixon 2015; Gaspari et al. 2017, 2018). This mechanism, where cold clouds condense from turbulence in the hot halo of galaxies, is observed in early-type galaxies typically residing in dense environments such as clusters and groups (e.g. Tremblay et al. 2016; Maccagni et al. 2018; Juráňová et al. 2019; Storchi-Bergmann & Schnorr-Müller 2019; Nagai et al. 2019). Given the distribution of the cold gas in the group of Fornax A, and the evidence for the occurrence of multiple interaction events, it is possible that one of these triggering mechanisms, or a combination of the two, regulates the flickering activity of Fornax A.

8. Summary and conclusions

Here we present new observations of Fornax A taken at ∼1 GHz with MeerKAT and at ∼6 GHz with the SRT. We used these data, along with archival observations of this source between 84 MHz and 217 GHz, to characterise the flux density distribution of the lobes and of the central emission of Fornax A. The spectral modelling of these components revealed that the lobes are not currently being replenished with energetic particles, and that this activity ceased about 12 Myr ago. In the centre, the central emission is not the remnant of the active phases that formed the lobes, but is tracing more recent activity of the AGN. The radiative ageing along the jets suggests that the injection phase was short ($\lesssim$1 Myr), and that the jets have been off for most of their lifetime ($t_{\rm OFF} \sim 2$ Myr).

The MeerKAT observation allowed us to obtain crucial information about the lobes of Fornax A and their spectral properties. The filaments appear embedded in a diffuse cocoon forming a double-shell structure. The outer edges of this shell with respect to the AGN have flat spectrum and high break frequency (see

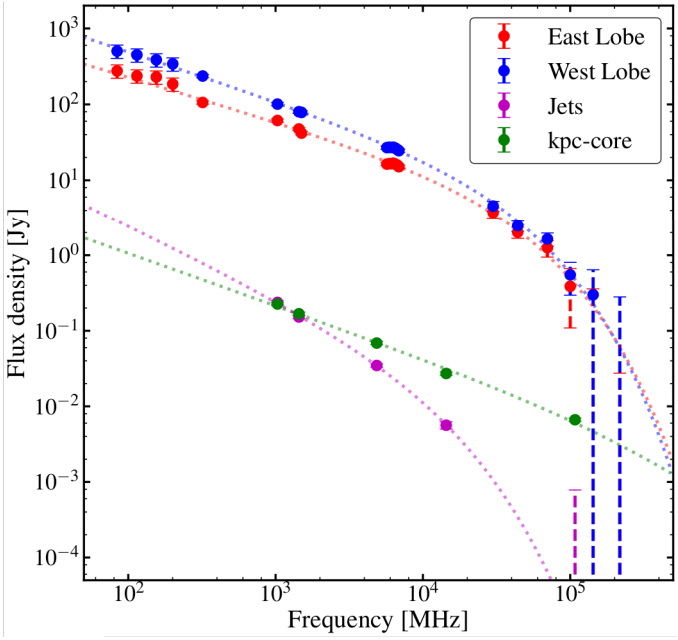

Fig. 15. Radio spectrum of the different components of Fornax A. The east lobe is shown in red, the west lobe in blue. The jets and kpc-core are in magenta and green, respectively. The dashed lines show the model of injection that best fits the flux distributions. The spectral shape of the lobes is very different from that of the inner components.

Figs. 9 and 12), while the inner regions and the bridge connecting the lobes show steep spectrum and lower break frequency. The comparison between the radiative age of the lobes and the dynamical age (Fig. 14) suggests that multiple nuclear activities inflated the lobes with high-energy particles, and that currently we are measuring the radiative age of the last of these recurrent episodes, which may also explain the double-shell morphology of the lobes.

The spectra of the kpc-core and jets (Fig. 8) suggest that the recent nuclear activity that formed them was shorter and likely less powerful than the previous one that inflated the lobes. As shown in Fig. 15, currently in Fornax A it is possible to observe three distinct phases of activity: the remnant phase that last injected the lobes, the more recent phase that generated the jets, and the current activity of the kpc-core. Given the short timescales of the nuclear activities we identified, Fornax A is likely rapidly flickering from an active nuclear phase to a non-active one.

Further information about the recurrent activity of Fornax A and, in particular about the last activity that generated the central emission, may be found in the study of the kinematics and distribution of the cold gas in the centre of the galaxy, along the jets. There, the molecular gas shows kinematics deviating from regular rotation, suggesting that part of the gas may be involved in the feeding of the AGN (Morokuma-Matsui et al. 2019). Neutral hydrogen clouds have also been detected at the same locations as the molecular gas (Serra et al. 2019). The analysis of its distribution and kinematics in relation to the nuclear activity of Fornax A will be presented in a following paper.

Acknowledgements. This paper is dedicated to the memory of Sergio Colafrancesco. The authors thank the anonymous referee for the useful comments and suggestions. The authors wish to thank Fernando Camilo for useful comments on an early draft of this paper. We are grateful to the full MeerKAT team at SARAO for their work on building and commissioning MeerKAT. This project has received funding from the European Research Council (ERC) under the European Union's Horizon 2020 research and innovation programme (grant agreement no. 679627). PK is partially supported by the BMBF project 05A17PC2 for D-MeerKAT. The MeerKAT telescope is operated by the South African Radio Astronomy Observatory, which is a facility of the National Research Foundation, an agency of the Department of Science and Innovation. The development of the SARDARA backend has been funded by the Autonomous Region of Sardinia (RAS) using resources from the Regional Law 7/2007 "Promotion of the scientific research and technological innovation in Sardinia" in the context of the research project CRP-49231 (year 2011, PI Possenti): "High resolution sampling of the Universe in the radio band: an unprecedented instrument to understand the fundamental laws of the nature". This paper makes use of the following ALMA data: ADS/JAO.ALMA#2017.1.00129.S. ALMA is a partnership of ESO (representing its member states). NSF (USA) and NINS (Japan), together with NRC (Canada), MOST and ASAIA (Taiwan), and KASI (Republic of Korea), in cooperation with the Republic of Chile. The Joint ALMA Observatory is operated by ESO, AUI/NRAO and NAOJ. The VLA images at 4.8 and 14.4 GHz have been produced as part of the NRAO VLA Archive Survey, (c) AUI/NRAO. The National Radio Astronomy Observatory (NRAO) is a facility of the National Science Foundation, operated under cooperative agreement by Associated Universities, Inc.

References

Ackermann, M., Ajello, M., Baldini, L., et al. 2016, ApJ, 826, 1
Anderson, C. S., Gaensler, B. M., Heald, G. H., et al. 2018, ApJ, 855, 41
Asad, K. M. B., Girard, J. N., de Villers, M., et al. 2019, MNRAS, submitted [arXiv:1904.07155]
Baars, J. W. M., Genzel, R., Pauliny-Toth, I. I. K., & Witzel, A. 1977, A&A, 500, 135
Battistelli, E. S., Fatigoni, S., Murgia, M., et al. 2019, ApJ, 877, L31
Bennett, C. L., Larson, D., Weiland, J. L., et al. 2013, ApJS, 208, 20
Bernardi, G., Greenhill, L. J., Mitchell, D. A., et al. 2013, ApJ, 771, 105
Bolatto, A. D., Warren, S. R., Leroy, A. K., et al. 2013, Nature, 499, 450
Bolli, P., Orlati, A., Stringhetti, L., et al. 2015, J. Astron. Instrum., 4, 1550008
Booth, C. M., & Schaye, J. 2009, MNRAS, 398, 53
Bower, R. G., Benson, A. J., Malbon, R., et al. 2006, MNRAS, 370, 645
Bridle, A. H., & Perley, R. A. 1984, ARA&A, 22, 319
Bridle, A. H., Baum, S. A., Fomalont, E. B., et al. 1991, A&A, 245, 371
Brienza, M., Godfrey, L., Morganti, R., et al. 2016, A&A, 585, A29
Brienza, M., Morganti, R., Murgia, M., et al. 2018, A&A, 618, A45
Cameron, M. J. 1971, MNRAS, 152, 439
Camilo, F., Scholz, P., Serylak, M., et al. 2018, ApJ, 856, 180
Cantiello, M., Grado, A., Blakeslee, J. P., et al. 2013, A&A, 552, A106
Carilli, C. L., Perley, R. A., Dreher, J. W., & Leahy, J. P. 1991, ApJ, 383, 554
Carlqvist, P. 2010, Ap&SS, 327, 267
Churazov, E., Brüggen, M., Kaiser, C. R., Böhringer, H., & Forman, W. 2001, ApJ, 554, 261
Ciotti, L., & Ziaee Lorzad, A. 2018, MNRAS, 473, 5476
Ciotti, L., Ostriker, J. P., & Proga, D. 2010, ApJ, 717, 708
Comerford, J. M., Barrows, R. S., Müller-Sánchez, F., et al. 2017, ApJ, 849, 102
Croton, D. J., Springel, V., White, S. D. M., et al. 2006, MNRAS, 365, 11
de Gasperin, F., Orrú, E., Murgia, M., et al. 2012, A&A, 547, A56
de Gasperin, F., Intema, H. T., Williams, W., et al. 2014, MNRAS, 440, 1542
Dolag, K., & Enßlin, T. A. 2000, A&A, 362, 151
Donohoe, J., & Smith, M. D. 2016, MNRAS, 458, 558
Drinkwater, M. J., Gregg, M. D., & Colless, M. 2001, ApJ, 548, L139
Duah Asabere, B., Horellou, C., Jarrett, T. H., & Winkler, H. 2016, A&A, 592, A20
Egron, E., Pellizzoni, A., Iacolina, M. N., et al. 2017, MNRAS, 470, 1329
Ekers, R. D., Goss, W. M., Wellington, K. J., et al. 1983, A&A, 127, 361
Ellis, G. R. A., & Hamilton, P. A. 1966, ApJ, 143, 227
Fabian, A. C. 2012, ARA&A, 50, 455
Fanaroff, B. L., & Riley, J. M. 1974, MNRAS, 167, 31P
Finlay, E. A., & Jones, B. B. 1973, Aust. J. Phys., 26, 389
Fluetsch, A., Maiolino, R., Carniani, S., et al. 2019, MNRAS, 483, 4586
Fomalont, E. B., Ebneter, K. A., van Breugel, W. J. M., & Ekers, R. D. 1989, ApJ, 346, L17
Galametz, M., Kennicutt, R. C., Albrecht, M., et al. 2012, MNRAS, 425, 763
Galametz, M., Albrecht, M., Kennicutt, R., et al. 2014, MNRAS, 439, 2542
Gardner, F. F., & Whiteoak, J. B. 1971, Aust. J. Phys., 24, 899
Gaspari, M., Ruszkowski, M., & Oh, S. P. 2013, MNRAS, 432, 3401
Gaspari, M., Temi, P., & Brighenti, F. 2017, MNRAS, 466, 677
Gaspari, M., McDonald, M., Hamer, S. L., et al. 2018, ApJ, 854, 167
Gaspari, M., Eckert, D., Ettori, S., et al. 2019, ApJ, 884, 169
Geldzahler, B. J., & Fomalont, E. B. 1978, AJ, 83, 1047

Geldzahler, B. J., & Fomalont, E. B. 1984, AJ, 89, 1650
Gizani, N. A. B., & Leahy, J. P. 2003, MNRAS, 342, 399
Goudfrooij, P., Mack, J., Kissler-Patig, M., Meylan, G., & Minniti, D. 2001, MNRAS, 322, 643
Grillmair, C. J., Forbes, D. A., Brodie, J. P., & Elson, R. A. W. 1999, AJ, 117, 167
Hardcastle, M. J., & Worrall, D. M. 2000, MNRAS, 319, 562
Harwood, J. J., Hardcastle, M. J., Croston, J. H., & Goodger, J. L. 2013, MNRAS, 435, 3353
Heckman, T. M., Smith, E. P., Baum, S. A., et al. 1986, ApJ, 311, 526
Hogan, M. T., Edge, A. C., Geach, J. E., et al. 2015, MNRAS, 453, 1223
Hopkins, P. F., Hernquist, L., Cox, T. J., et al. 2005, ApJ, 630, 705
Horellou, C., Black, J. H., van Gorkom, J. H., et al. 2001, A&A, 376, 837
Hurley-Walker, N., Callingham, J. R., Hancock, P. J., et al. 2017, MNRAS, 464, 1146
Iodice, E., Spavone, M., Capaccioli, M., et al. 2017, ApJ, 839, 21
Isobe, N., Makishima, K., Tashiro, M., et al. 2006, ApJ, 645, 256
Iyomoto, N., Makishima, K., Tashiro, M., et al. 1998, ApJ, 503, L31
Jaffe, W. J., & Perola, G. C. 1973, A&A, 26, 423
Jamrozy, M., Klein, U., Mack, K. H., Gregorini, L., & Parma, P. 2004, A&A, 427, 79
Jonas, J., & MeerKAT Team Proceedings of MeerKAT Science: On the Pathway to the SKA. 25–27 May, 1
Jones, D. L., & Preston, R. A. 2001, AJ, 122, 2940
Jones, P. A., & McAdam, W. B. 1992, ApJS, 80, 137
Jones, P. A., McAdam, W. B., & Reynolds, J. E. 1994, MNRAS, 268, 602
Józsa, G. I. G., Garrett, M. A., Oosterloo, T. A., et al. 2009, A&A, 500, L33
Juráňová, A., Werner, N., Gaspari, M., et al. 2019, MNRAS, 484, 2886
Kaneda, H., Tashiro, M., Ikebe, Y., et al. 1995, ApJ, 453, L13
Kardashev, N. S. 1962, Soviet Ast., 6, 317
King, A., & Nixon, C. 2015, MNRAS, 453, L46
Kolokythas, K., O'Sullivan, E., Giacintucci, S., et al. 2015, MNRAS, 450, 1732
Komissarov, S. S., & Gubanov, A. G. 1994, A&A, 285, 27
Krause, M. G. H., Shabala, S. S., Hardcastle, M. J., et al. 2019, MNRAS, 482, 240
Kuntschner, H. 2000, MNRAS, 315, 184
Kuźmicz, A., Jamrozy, M., Kozieł-Wierzbowska, D., & Weżgowiec, M. 2017, MNRAS, 471, 3806
Laing, R. A., Parma, P., de Ruiter, H. R., & Fanti, R. 1999, MNRAS, 306, 513
Lanz, L., Jones, C., Forman, W. R., et al. 2010, ApJ, 721, 1702
Leahy, J. P., & Williams, A. G. 1984, MNRAS, 210, 929
Lintott, C. J., Schawinski, K., Keel, W., et al. 2009, MNRAS, 399, 129
Maccagni, F. M., Morganti, R., Oosterloo, T. A., Oonk, J. B. R., & Emonts, B. H. C. 2018, A&A, 614, A42
Mackie, G., & Fabbiano, G. 1998, AJ, 115, 514
Marconi, A., Risaliti, G., Gilli, R., et al. 2004, MNRAS, 351, 169
Matthews, J. H., Bell, A. R., Blundell, K. M., & Araudo, A. T. 2019, MNRAS, 482, 4303
McGee, R. X., Slee, O. B., & Stanley, G. J. 1955, Aust. J. Phys., 8, 347
McKinley, B., Yang, R., López-Caniego, M., et al. 2015, MNRAS, 446, 3478
McNamara, B. R., & Nulsen, P. E. J. 2012, New J. Phys., 14, 055023
Melis, A., Concu, R., Trois, A., et al. 2018, JAI, 7, 1850004
Monceau-Baroux, R., Porth, O., Meliani, Z., & Keppens, R. 2014, A&A, 561, A30
Morganti, R. 2017, Nat. Astron., 1, 596
Morganti, R., Killeen, N. E. B., & Tadhunter, C. N. 1993, MNRAS, 263, 1023
Morokuma-Matsui, K., Serra, P., Maccagni, F. M., et al. 2019, PASJ, 71, 85
Mullin, L. M., Riley, J. M., & Hardcastle, M. J. 2008, MNRAS, 390, 595
Murgia, M. 2003, PASA, 20, 19
Murgia, M., Fanti, C., Fanti, R., et al. 1999, A&A, 345, 769
Murgia, M., Govoni, F., Feretti, L., & Giovannini, G. 2010a, A&A, 509, A86
Murgia, M., Eckert, D., Govoni, F., et al. 2010b, A&A, 514, A76
Murgia, M., Parma, P., Mack, K. H., et al. 2011, A&A, 526, A148
Murgia, M., Markevitch, M., Govoni, F., et al. 2012, A&A, 548, A75
Murgia, M., Govoni, F., Carretti, E., et al. 2016, MNRAS, 461, 3516
Myers, S. T., & Spangler, S. R. 1985, ApJ, 291, 52
Nagai, H., Onishi, K., Kawakatu, N., et al. 2019, ApJ, 883, 193
Nagino, R., & Matsushita, K. 2009, A&A, 501, 157
Noordam, J. E., & Smirnov, O. M. 2010, A&A, 524, A61
Offringa, A. R., & Smirnov, O. 2017, MNRAS, 471, 301
Offringa, A. R., McKinley, B., Hurley-Walker, N., et al. 2014, MNRAS, 444, 606
Orrù, E., Murgia, M., Feretti, L., et al. 2010, A&A, 515, A50
Pacholczyk, A. G. 1970, Radio Astrophysics. Nonthermal Processes in Galactic and Extragalactic Sources
Parma, P., Fanti, C., Fanti, R., Morganti, R., & de Ruiter, H. R. 1987, A&A, 181, 244
Parma, P., Murgia, M., Morganti, R., et al. 1999, A&A, 344, 7
Parma, P., Murgia, M., de Ruiter, H. R., et al. 2007, A&A, 470, 875
Partridge, B., López-Caniego, M., Perley, R. A., et al. 2016, ApJ, 821, 61
Perley, R. A., & Butler, B. J. 2013a, ApJS, 204, 19
Perley, R. A., & Butler, B. J. 2013b, ApJS, 206, 16
Perley, R. A., & Butler, B. J. 2017, ApJS, 230, 7
Petry, D., & CASA Development Team, ASP Conf. Ser., 461, 849
Piddington, J. H., & Trent, G. H. 1956, Aust. J. Phys., 9, 481
Planck Collaboration XI. 2014, A&A, 571, A11
Planck Collaboration I. 2016, A&A, 594, A1
Planck Collaboration X. 2016, A&A, 594, A10
Planck Collaboration IV. 2020, A&A, in press, https://doi.org/10.1051/0004-6361/201833881
Planck Collaboration Int. XLVIII. 2016, A&A, 596, A109
Prandoni, I., Murgia, M., Tarchi, A., et al. 2017, A&A, 608, A40
Ramos Almeida, C., Bessiere, P. S., Tadhunter, C. N., et al. 2012, MNRAS, 419, 687
Roussel, H., Helou, G., Hollenbach, D. J., et al. 2007, ApJ, 669, 959
Sabater, J., Best, P. N., & Argudo-Fernández, M. 2013, MNRAS, 430, 638
Saikia, D. J., & Jamrozy, M. 2009, Bull. Astron. Soc. India, 37, 63
Schawinski, K., Koss, M., Berney, S., & Sartori, L. F. 2015, MNRAS, 451, 2517
Schweizer, F. 1980, ApJ, 237, 303
Serra, P., de Blok, W. J. G., Bryan, G. L., et al. 2016, Proceedings of MeerKAT Science: On the Pathway to the SKA. 25–27 May, 8
Serra, P., Westmeier, T., Giese, N., et al. 2015, MNRAS, 448, 1922
Serra, P., Maccagni, F. M., Kleiner, D., et al. 2019, A&A, 628, A122
Sesto, L. A., Faifer, F. R., & Forte, J. C. 2016, MNRAS, 461, 4260
Sesto, L. A., Faifer, F. R., Smith Castelli, A. V., Forte, J. C., & Escudero, C. G. 2018, MNRAS, 479, 478
Seta, H., Tashiro, M. S., & Inoue, S. 2013, PASJ, 65, 106
Shabala, S. S., Deller, A., Kaviraj, S., et al. 2017, MNRAS, 464, 4706
Shain, C. A. 1958, Aust. J. Phys., 11, 517
Shain, C. A., & Higgins, C. S. 1954, Aust. J. Phys., 7, 130
Shimmins, A. J. 1971, Aust. J. Phys. Astrophys. Suppl., 21, 1
Shulevski, A., Morganti, R., Oosterloo, T., & Struve, C. 2012, A&A, 545, A91
Silva, D. R., Kuntschner, H., & Lyubenova, M. 2008, ApJ, 674, 194
Slee, O. B., Sadler, E. M., Reynolds, J. E., & Ekers, R. D. 1994, MNRAS, 269, 928
Slee, O. B., Roy, A. L., Murgia, M., Andernach, H., & Ehle, M. 2001, AJ, 122, 1172
Stanghellini, C., O'Dea, C. P., Dallacasa, D., et al. 2005, A&A, 443, 891
Storchi-Bergmann, T., & Schnorr-Müller, A. 2019, Nat. Astron., 3, 48
Tadhunter, C. N., Morganti, R., di Serego Alighieri, S., Fosbury, R. A. E., & Danziger, I. J. 1993, MNRAS, 263, 999
Tashiro, M. S., Isobe, N., Seta, H., Matsuta, K., & Yaji, Y. 2009, PASJ, 61, S327
Tremblay, G. R., Oonk, J. B. R., Combes, F., et al. 2016, Nature, 534, 218
Woltjer, L. 1959, ApJ, 130, 38

Appendix A: Continuum images of Fornax A from archival data

A.1. MWA: 84–230 MHz

To characterise the radio spectrum of Fornax A at low frequencies (84–200 MHz) we select MWA archival observations from the GLEAM survey. The images are shown in Fig. A.1. As reported by McKinley et al. (2015), self-calibration is known to affect the flux-density scale of MWA images of Fornax A. For this reason in their work on Fornax A, these latter authors calculated a flux-scaling factor of 1.325. We apply the same scaling factor to our flux measurements obtaining compatible results (see Table B.1 and Fig. B.1).

A.2. VLA: p-band, 1500, 4800 MHz and 14.4 GHz

We select VLA observations of Fornax A to analyse both the flux density of the lobes (at 320 MHz and 1500 MHz) and the central emission of Fornax A (at 4.8 GHz and 14.4 GHz). The bandwidth, PSF and noise of the images are summarised in Table 2. The *p*-band observations of Fornax A were taken on May 12 1989 with configurations B and C. The total integration time was 2.5 h. For the purposes of this work, we performed a new data reduction. Calibration and imaging were performed with the Astronomical Image Processing System (`AIPS`). De-convolution was done with multi-scale cleaning, and direction-dependent calibration has been used in the self-calibration phase. The resulting continuum image is shown in the left panel of Fig. A.2.

The image at 1500 MHz shown in the right panel of the figure as presented for the first time in Fomalont et al. (1989). It is the mosaic of multiple pointings centred on the lobes, with all VLA configurations.

As illustrated in Sect. 2, the highest-resolution observations are chosen to study the central radio emission. Both images at 4.8 GHz and 14.4 GHz (see Fig. 4) were taken from the NRAO VLA archive survey images[5] without applying any further modification. The image at 4.8 GHz was produced on February 21, 2007, from observations taken on October 6, 2002. The image at 14.4 GHz was produced on March 6, 2007, from observations taken on January 24, 2002.

A.3. Planck: 30 GHz–217 GHz

We obtained images of Fornax A at 30, 44, 70, 100, 143 and 217 GHz analysing the final release of the *Planck* foreground maps (Planck Collaboration IV 2020). From these maps, we cut out an image four degrees wide centred on Fornax A.

At frequencies $\gtrsim$100 GHz thermal dust emission dominates over the non-thermal emission (Planck Collaboration XI 2014; Planck Collaboration X 2016). The *Planck* collaboration released full-mission maps of the thermal dust component at 353 GHz, 545 GHz and 857 GHz (Planck Collaboration IV 2020). The separation of the thermal dust emission from the other components can be done using different methods (Planck Collaboration X 2016; Planck Collaboration Int. XLVIII 2016). Here, we use the products of the Generalized Needlet Internal Linear Combination (GNILC) component separation presented in Planck Collaboration Int. XLVIII (2016). The SED of thermal dust is well described by a modified blackbody:

$$I_\nu = \tau_{\nu_0} B_\nu(T_{\rm obs}) \left(\frac{\nu}{\nu_0}\right)^{\beta_{\rm obs}}, \tag{A.1}$$

where $\nu_0 = 345$ GHz is the reference frequency at which the optical depth τ_{ν_0} is estimated, $\beta_{\rm obs}$ is the spectral index of the dust and $T_{\rm obs}$ its temperature. $B_\nu(T_{\rm obs})$ indicates the flux density of the blackbody. Using the maps of the optical depth, temperature, and spectral index of the dust emission (Planck Collaboration IV 2020) produced by the GNILC component separation including also IRAS observations at 100 μm, we produced maps of the dust thermal emission at 100 GHz, 143 GHz, and 217 GHz. These maps were subtracted pixel by pixel from the archival foreground emission maps.

Analogously to the dust, free-free emission also contributes diffuse foreground emission and needs to be subtracted from the *Planck* maps to determine the correct flux density of Fornax A. Using the maps of emission measure and electron temperature (Planck Collaboration X 2016; Planck Collaboration IV 2020) produced by the GNILC component separation, we generated maps of the free-free emission at all HFI frequencies, and we subtracted them from the foreground dust-subtracted maps.

Besides the thermal dust and the free-free components, the Cosmic Infrared Background (CIB) also contributes to the flux of the *Planck* foreground maps. Since this component is diffuse on scales larger than Fornax A, we corrected the images of Fornax A subtracting the average value of the CIB reported in Planck Collaboration I (2016).

Planck images are released in `HEALPix` format, in units of $T_{\rm CMB}$ (i.e. CMB anisotropies, $\Delta T/T$). We regridded the images to `WCS` projection in equatorial coordinates, and we converted them to units of MJy/sr as follows:

$$S_{\nu_{\rm obs}}\,[\mathrm{MJy/sr}] = S_{\nu_{\rm obs}}\,[T_{\rm CMB}] \times 10^4 \cdot \frac{C}{T_{\rm CMB}} \frac{\sigma}{e^x} \cdot \frac{x\,e^x}{e^x - 1}, \tag{A.2}$$

where $\sigma = \nu_{\rm obs}/29.979$, $x = 1.4388\sigma/T_{\rm CMB}$, $T_{\rm CMB} = 2.725$ K and $C = 2.99 \times 10^{10}$ cm s^{-1}. Then:

$$S_{\nu_{\rm obs}}\,[\mathrm{Jy\,beam^{-1}}] = 2.350443 \times 10^{-5} \cdot S_{\nu_{\rm obs}}\,[\mathrm{MJy\,sr^{-1}}] \times 2\pi \frac{\Theta_{{\rm maj},\nu}['']}{2.35482} \frac{\Theta_{{\rm min},\nu}['']}{2.35482}. \tag{A.3}$$

Figure A.3 shows the centre of the field of view of the *Planck* images of Fornax A between 30 and 217 GHz in units of Jy beam^{-1}, subtracted of the dust, free-free and CIB backgrounds. In the LFI band the lobes of Fornax A are unresolved, or resolved with at most one resolution element (70 GHz), in the HFI band the lobes are resolved, but fall below the sensitivity of the observations at $\gtrsim$143 GHz.

As illustrated in Sect. 2, the noise in the *Planck* images surrounding Fornax A is not white. Hence, to make a reliable estimate on the error on the flux of Fornax A, we measure the noise as the standard deviation from the average flux density measured in the field of view in 100 regions of the same size of the lobes of Fornax A (Fig. A.3).

[5] http://www.aoc.nrao.edu/~vlbacald/ArchIndex.shtml

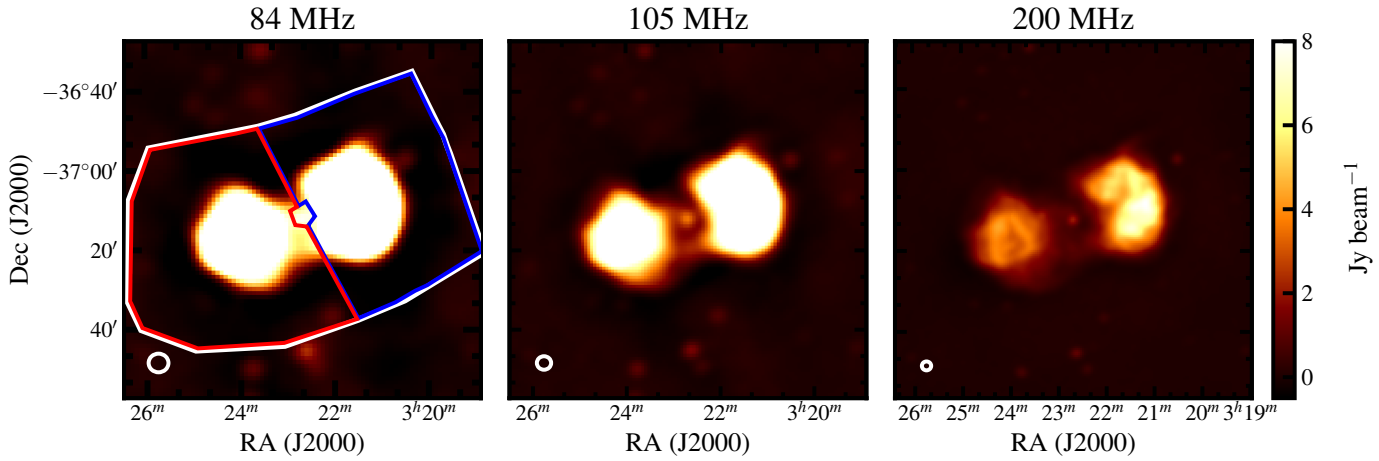

Fig. A.1. Fornax A seen by the MWA between 70 MHz and 230 MHz. The colour-scale is the same in all panels. In the *left panel*, the white contours mark the region where we measure the total flux of the source, the red and blue contours show the regions of the east and west lobes. The PSF of the images is shown in white in the bottom left corner.

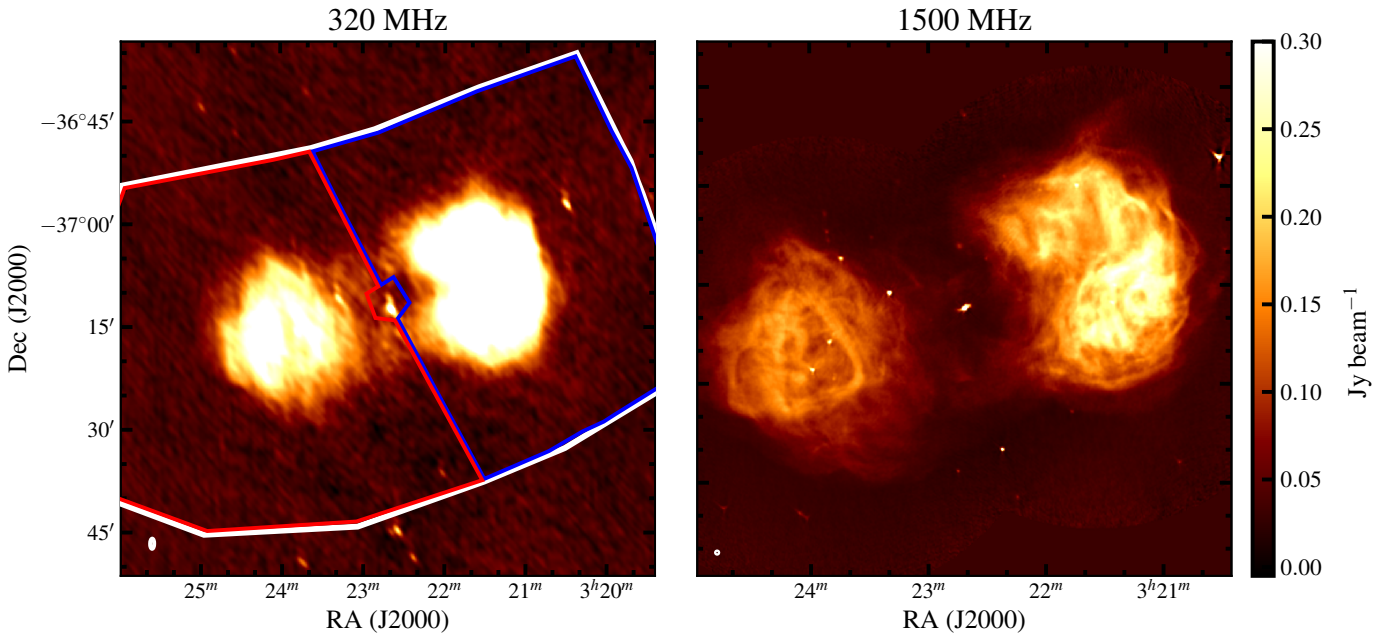

Fig. A.2. Fornax A seen by the VLA at 320 MHz and 1500 MHz. The colour-scale is the same in both panels. As in the previous figures, the regions in the *left panel* show where we measure the flux density of the radio lobes. The PSF of the images is shown in white in the bottom left corner.

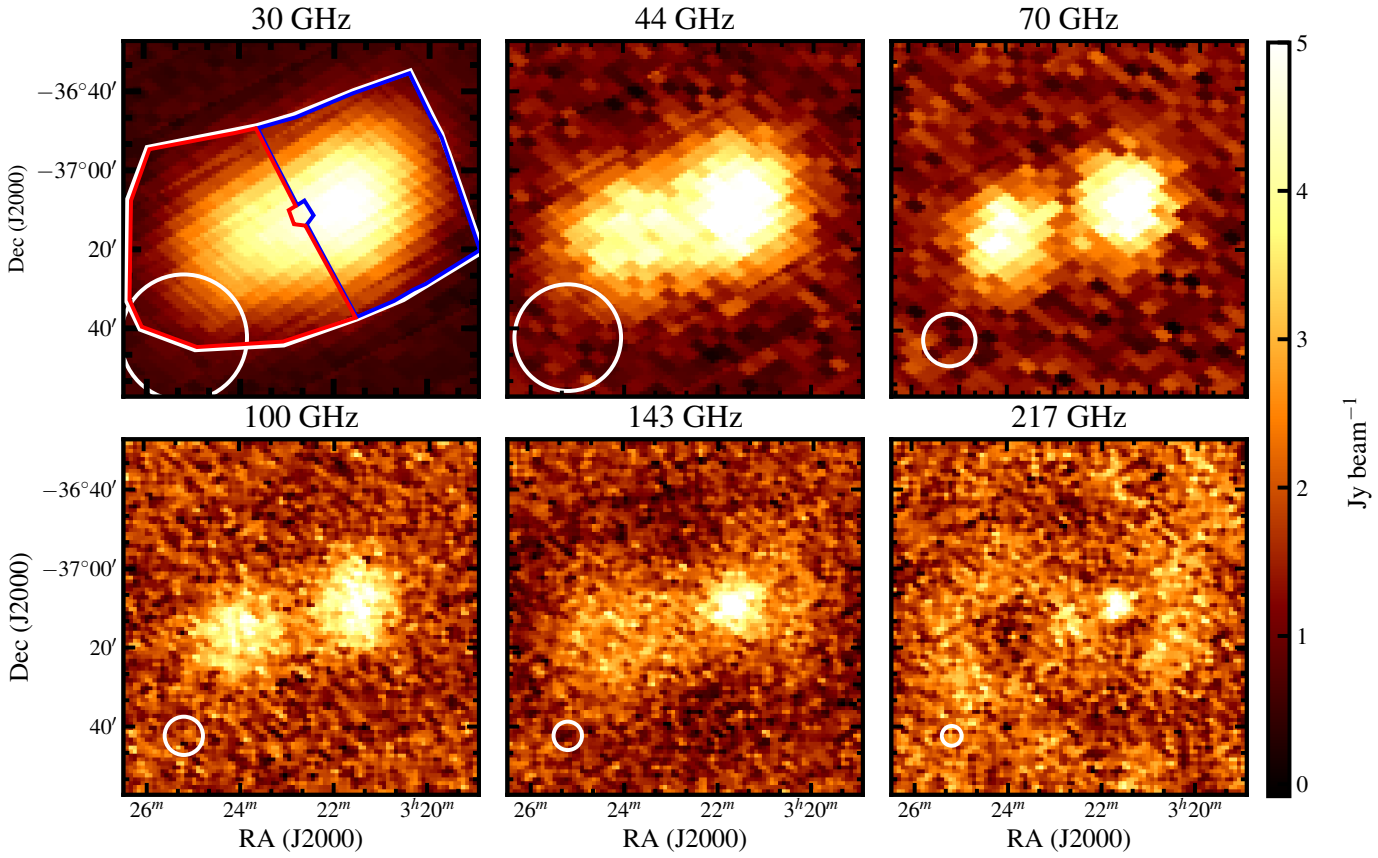

Fig. A.3. Fornax A seen by the *Planck* LFI at 30, 44 and 70 GHz, and by *Planck* HFI at 100, 144 and 217 GHz. At 217 GHz the lobes of Fornax A are undetected. The colour-scale is the same in all panels. The PSF of the images is shown in white in the bottom left corner. The blue and red regions in the *top left panel* indicate where we measure the flux density of the east and west lobes.

Appendix B: The total flux density distribution of Fornax A

In Table B.1 we show the total flux density distribution of Fornax A measured in this work along with the previously published measurements of McKinley et al. (2015) and Perley & Butler (2017). McKinley et al. (2015) show the spectrum of Fornax A between 4.7 MHz and 1.3×10^{18} MHz, making use of archival observations as well as new MWA, WMAP, *Planck* and *Fermi*-LAT observations. Perley & Butler (2017) focus in extending the flux calibration scale of Fornax A between 200 and 500 MHz. As shown in Fig. B.1, the measurements of the total flux density of Fornax A presented in this work are compatible within the errors with the measurements previously published. The left panel of the figure shows that the flux measured at 1.50 GHz by the VLA is slightly lower than what expected, compared to the MeerKAT measurement at 1.44 GHz. It is possible that the limited coverage of the VLA over short baselines misses part of the flux of the lobes ($\lesssim$5%). The measurements in the low SRT frequencies ($\nu \lesssim 6300$ MHz) also seem not to be compatible with the monotonous trend of the spectrum from synchrotron radiation. These errors may be caused by the opacity correction we applied (Eq. (1)), that does not take into account the frequency-dependence of the opacity. This may lead to underestimation of the flux in the low-frequency end of the band. These errors are negligible for the purposes of this study. We point out that this correction becomes important at SRT only for low-elevation observations, such as the one of Fornax A.

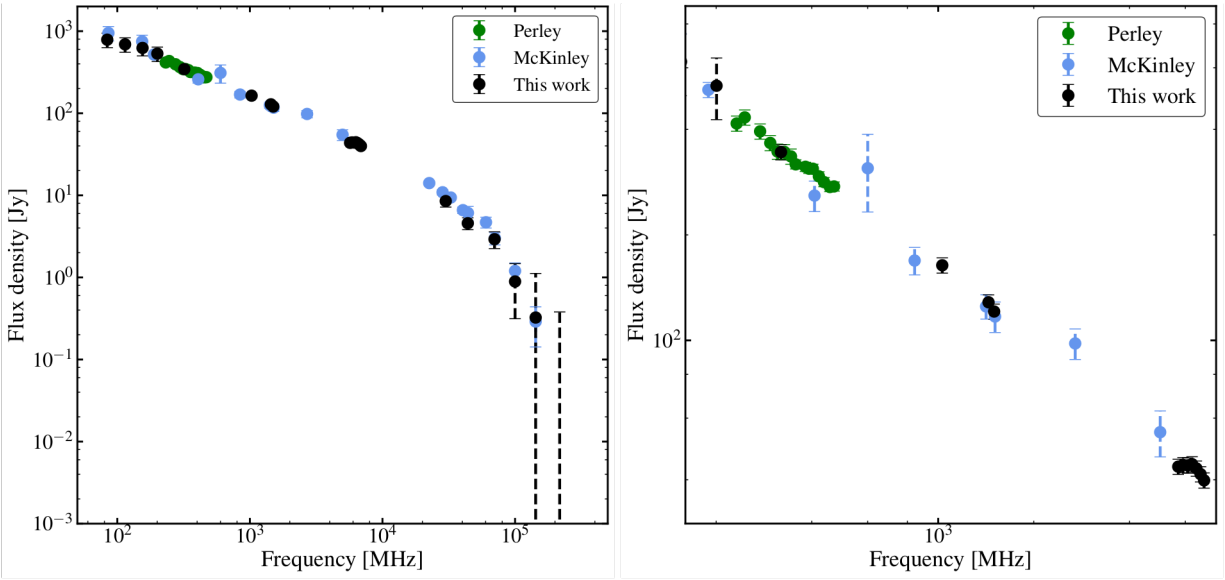

Fig. B.1. *Left panel*: total flux density distribution of Fornax A between 84 MHz and 217 GHz measured in this work (black), between 4.7 MHz and 143 GHz by McKinley et al. (2015) (blue) and between 232 MHz and 470 MHz by Perley & Butler (2017) (green). *Right panel*: zoom of the left panel between 200 MHz and 7 GHz, the bandwidth used to make the spectral index maps discussed in Sect. 5.1.

Table B.1. Total flux density of Fornax A.

Frequency [GHz]	Flux density (this work) [Jy]	Flux density (McK) [Jy]	Flux density (PeR) [Jy]	Telescope/Reference [–]
4.70×10^{-3}		13500±20% (*)		Ellis & Hamilton (1966)
1.83×10^{-2}		3500±20%		Shain & Higgins (1954)
1.97×10^{-2}		4300±20%		Shain (1958)
2.99×10^{-2}		2120±10%		Finlay & Jones (1973)
8.40×10^{-2}	788 ± 158	950±20%		MWA
0.118	692 ± 138			MWA
0.154	642 ± 125	750±19%		MWA
0.189		519±5% (*)		Bernardi et al. (2013)
0.200	533 ± 107			MWA
0.232			416±5%	VLA
0.246			433±5%	VLA
0.275			395±5%	VLA
0.296			366±5%	VLA
0.312			346±5%	VLA
0.320	343 ± 17			VLA
0.328			345±5%	VLA
0.344			335±5%	VLA
0.356			318±3%	VLA
0.382			313±3%	VLA
0.392			309±3%	VLA
0.400		140±10% (*)		McGee et al. (1955)
0.403			309±3%	VLA
0.408		259±10%		Cameron (1971)
0.421			294±3%	VLA
0.437			283±3%	VLA
0.456			274±3%	VLA
0.470			275±3%	VLA
0.600		310±25%		Piddington & Trent (1956)
0.843		169±9%		Jones & McAdam (1992)
1.03	163 ± 8			MeerKAT
1.42		125±8%		VLA
1.44	128 ± 6			MeerKAT
1.50	121 ± 6	117±10%		VLA
2.70		98±10%		Shimmins (1971)
5.00		54±5%		Gardner & Whiteoak (1971)
5.70	44 ± 2			SRT
5.90	44 ± 2			SRT
6.10	44 ± 2			SRT
6.30	44 ± 2			SRT
6.50	43 ± 2			SRT
6.70	41 ± 2			SRT
6.87	39 ± 1			SRT
22.5		14±5%		WMAP(†)
30.0	8.5 ± 1.3	11±7%		*Planck*
32.8		9.4±6%		WMAP
40.4		6.6±9%		*Planck*
44.0	4.6 ± 0.7	6.1±20%		WMAP
60.4		4.7±15%		WMAP
70.0	2.9 ± 0.5	3.0±17%		*Planck*
100	0.9 ± 0.4	1.2±25%		*Planck*
143	0.3 ± 0.5	0.29±51%		*Planck*
217	(0.7)			*Planck*

Notes. Column (1) shows the frequencies at which we measure the flux density of Fornax A. Column (2) shows the flux densities measured in this work. Column (3) shows the flux densities shown in McKinley et al. (2015). Column (4) shows the flux densities shown in Perley & Butler (2017). Column (5) indicates the telescope used for the measurements, or the reference to the published fluxes. (*)indicates flux densities that have not been included in the study of the SED. (†)WMAP: *Wilkinson* Microwave Anisotropy Probe (Bennett et al. 2013).